CHALMERS
UNIVERSITY OF TECHNOLOGY

Corrosivity of KOH(g) towards superheater materials in a simulated air reactor environment for chemical looping combustion of biomass

Downloaded from: https://research.chalmers.se, 2024-11-19 05:14 UTC

Citation for the original published paper (version of record):
Lindmark, H., Faust, R., Sand, T. et al (2025). Corrosivity of KOH(g) towards superheater materials in a simulated air reactor environment for
chemical looping combustion of biomass. Fuel, 381. http://dx.doi.org/10.1016/j.fuel.2024.133178

N.B. When citing this work, cite the original published paper.

research.chalmers.se offers the possibility of retrieving research publications produced at Chalmers University of Technology. It covers all kind of research output: articles, dissertations, conference papers, reports etc. since 2004. research.chalmers.se is administrated and maintained by Chalmers Library

(article starts on next page)

Fuel 381 (2025) 133178

Contents lists available at ScienceDirect

Fuel

journal homepage: www.elsevier.com/locate/fuel

Full Length Article

Corrosivity of KOH(g) towards superheater materials in a simulated air reactor environment for chemical looping combustion of biomass

Hampus Lindmark [a,*], Robin Faust [a], Tommy Sand [b], Lars-Gunnar Johansson [a], Pavleta Knutsson [a], Jesper Liske [a]

[a] Department of Chemistry and Chemical Engineering, Chalmers University of Technology, Kemigården 4, 41296 Gothenburg, Sweden
[b] Alleima Tube AB, Storgatan 2, 811 81, Sandviken, Sweden

ARTICLE INFO

Keywords:
Chemical looping combustion
Biomass
High-temperature corrosion
KOH
Stainless steels
Ni-base alloys
FeCrAl alloys

ABSTRACT

Chemical looping combustion (CLC) of biomass has the potential to improve the electrical efficiency in power plants that utilize carbon capture and storage (CCS). This is attributed to the mild corrosive environment anticipated in the air reactor (AR). However, previous studies have measured alkali emissions in the AR, likely in the form of KOH(g), suggesting that alkali may transfer from the fuel reactor (FR) to the AR. To investigate the corrosive effect of KOH(g) release in the AR, a novel experimental set-up was developed to simulate two scenarios for the AR 1) Clean scenario: no release of KOH(g) in the AR (5 % O_2 + 3 % H_2O + N_2 bal.) and 2) Alkali slip scenario: continuous release of KOH(g) in the AR (5 % O_2 + 3 % H_2O + N_2 bal. + 16 ppm KOH(g)). The exposure was carried out at 700 °C and six alloys, relevant as superheater material, ranging from stainless steels to nickel-base (Ni-base) alloys as well as a FeCrAl alloy were investigated. The samples were exposed for a total of 168 h and the morphology of the corrosion products was investigated using SEM-EDX and XRD. The presented results suggest that KOH(g) significantly accelerates the corrosion of the stainless steels and Ni-base alloys investigated, by rapidly destroying the protective Cr-rich oxide scale, resulting in the formation of a multilayer oxide scale with inferior protective properties. On the contrary, the FeCrAl alloy retained a protective Al-rich oxide scale irrespective of the presence of KOH(g). The findings in this study highlight that the release of KOH(g) in the AR during combustion of biomass in CLC could introduce corrosion challenges for installed superheaters that can be significantly mitigated by utilizing FeCrAl alloys.

1. Introduction

According to the International Panel on Climate Change (IPCC), a shift from a society dependent on fossil fuel to one powered by renewable energy sources is required to meet the targets of the Paris Agreement, aiming to restrict global warming to "well below 2 °C" [1]. In addition, to compensate for historic emissions and to offset hard-to-abate CO_2 sources, negative CO_2 emissions have been purposed to play a crucial role in achieving this target [1]. Negative CO_2 emissions can be accomplished by integrating bioenergy with carbon capture and storage (BECCS) where point emitters such as combined heat and power (CHP) plants are suitable CO_2 sources [1]. Biomass is categorized as CO_2-neutral fuel since the CO_2 emitted to the atmosphere during combustion is captured by the growing biomass through photosynthesis. By capturing the emitted CO_2 by the biomass conversion in point sources before it enters the atmosphere and storing it in geological storage locations, negative CO_2 emission can be achieved [2]. Previous studies have estimated the global potential of BECCS to range between 0.5 and 9.5 $GtCO_2$/year until 2050 [3].

Today, the only commercially available technology for large scale BECCS in CHP plants is the so-called post-combustion method [4]. This method is based on CO_2 absorbents (for example hot potassium carbonate (HPC) or amine-based scrubbers) through which the flue gas is led in a second reactor where temperature or pressure are changed thereby causing the absorbents to release the captured CO_2 that can subsequently be pressurized, transported and stored [4]. For instance, the Swedish utility company Stockholm Exergi is currently designing and building one of the world's first large-scale BECCS units, in connection to a CHP plant and based on the post-combustion HPC method, intending to capture 800 kt CO_2 annually [5]. Even though showing promising CO_2-capturing results, the post-combustion technique involves a large energy penalty associated with the regeneration of the absorbent, making it unsuitable for powerplants focusing on

* Corresponding author.
E-mail address: lhampus@chalmers.se (H. Lindmark).

https://doi.org/10.1016/j.fuel.2024.133178
Received 18 June 2024; Received in revised form 11 September 2024; Accepted 15 September 2024
Available online 4 October 2024
0016-2361/© 2024 The Author(s). Published by Elsevier Ltd. This is an open access article under the CC BY license (http://creativecommons.org/licenses/by/4.0/).

Nomenclature

AR	Air Reactor
BECCS	Bioenergy with Carbon Capture and Storage
BIB	Broad Ion Beam
BSE	Back Scattered Electrons
CHP	Combined Heat and Power
CLC	Chemical Looping Combustion
CO_2	*Carbon Dioxide*
CTE	Coefficient of Thermal Expansion
CuO	*Copper Oxide*
FR	Fuel Reactor
HCl	*Hydrochloric acid*
H_2O	*Water*
HPC	*Hot Potassium Carbonate*
IOZ	*Internal Oxidation Zone*
IPCC	*International Panel on Climate Change*
KCl	*Potassium Chloride*
K_2CO_3	*Potassium Carbonate*
keV	Kiloelectron Volt
$KFeO_2$	*Potassium Ferrate*
KOH	*Potassium Hydroxide*
Me_xO_y	*Oxidizing state of Oxygen Carrier*
Me_xO_{y-1}	*Reducing state of Oxygen Carrier*
N_2	*Nitrogen*
OC	*Oxygen Carrier*
SEM-EDX	Scanning Electron Microscope coupled with Energy Dispersive X-ray
SI	Supplementary Information
XRD	X-ray Diffraction

electricity generation [5–7].

Compared to the post-combustion method, the chemical looping combustion (CLC) technique offers a significantly reduced energy penalty for CO_2 gas separation while also potentially enabling an improved electrical efficiency during combustion of biomass. While no commercialized units are in place as of today, Lyngfeldt et al. report successful pilot-scale tests indicating the potential for scale-up [8]. CLC involves two interconnected fluidized bed reactors, the air reactor (AR) and the fuel reactor (FR), (see Fig. 1). Both reactors use a granular material which serves as both the bed material and as a so-called oxygen carrier (OC) and circulates between the two reactors [8]. In the AR, the OC undergoes oxidation (forming Me_xO_y) by reacting with air in a highly exothermic process. The OC are then transported to the FR where it undergoes reduction (forming Me_xO_{y-1}) by reacting with the fuel. The inherent design of CLC allows combustion to take place without the addition of air which produces a flue gas which is free of N_2 and predominantly consists of CO_2 and H_2O [8]. Consequently, the energy penalty for separating CO_2 from the flue gas is significantly lower compared to post-combustion methods. Rydén et al. suggest that CLC is expected to reduce the energy penalty associated with CO_2 gas separation by half when compared to other CO_2 capturing techniques [9].

In addition to superior CO_2 separation, CLC offers great potential in improving the electricity production during combustion of biomass. A major challenge associated with conventional biomass-fired boilers, where heat extraction and combustion take place in the same reactor, is the release of highly corrosive chemical species in the flue gas, including alkali-containing compounds such as KCl, NaCl, and K_2CO_3, as well as HCl(g) and H_2O(g) that upon interaction with the superheaters cause severe corrosion [10–20]. Consequently, to minimize the corrosion rate, boiler operators today are forced to keep the superheated steam at relatively low temperatures, corresponding to an electrical efficiency inferior to that when using traditional fossil fuels [21]. In CLC on the other hand, combustion and heat release are *inherently separated* from each other. Consequently, by positioning superheaters on the AR side, where no fuel is introduced, a less corrosive environment is expected. This would enable improved steam temperatures and extend the superheaters' lifetime, ultimately resulting in an improved electrical efficiency that could compete with coal-fired electricity production [22]. In a recent laboratory study, several high temperature materials performed well in simulated environments aiming to investigate the potential corrosion attack of future superheaters placed within the AR in CLC [23]. Even though no fuel-released alkali is expected in the AR, previous studies have reported that volatile alkali compounds may be carried over from the FR to the AR [24,25]. For instance, Gogolev et al. measured alkali emission in the AR to about 1 mg/Nm^3 of a biomass fueled 10 kW CLC pilot [26]. The potassium detected in the air reactor is suggested to originate solely from carryover processes, including the transfer of char and ash-deposited alkalis from the fuel reactor, as well as the carryover of potassium absorbed on the oxygen carrier [27]. Under the conditions present in the air reactor, potassium from char and ash is expected to be released as gaseous KOH, formed through the decomposition of alkali salts such as K_2CO_3 at high temperatures [27]. Potassium bound to ilmenite ($FeTiO_3$), a commonly used oxygen carrier in CLC, in the form of K-titanate phase ($KTi_8O_{16.5}$), could also theoretically contribute to KOH(g) release into the air reactor.

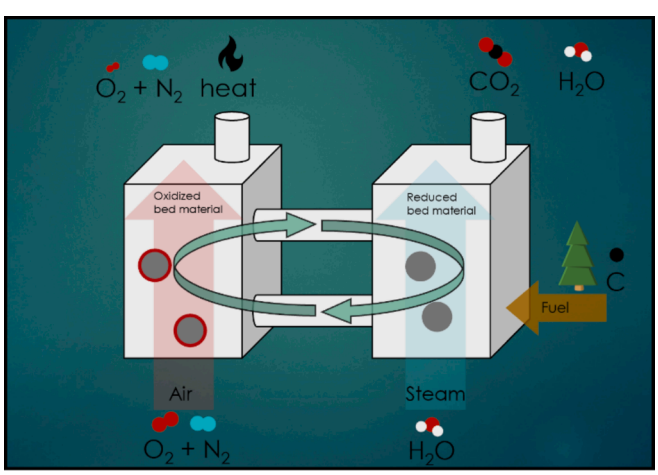

Fig. 1. Schematic depiction of chemical looping combustion (CLC) showing the air reactor (AR) on the left and the fuel reactor (FR) on the right.

Superheater tubes are usually composed of low alloyed carbon steels due to their low cost and good mechanical properties. However, these alloys offer limited corrosion resistance in the superheater regions of conventional biomass boilers. One method to reduce the corrosion rate of superheaters is to use alloys with high corrosion resistance, such as stainless steel. Alternatively, applying corrosion-resistant coatings or weld overlays—such as Ni-base coatings or Ni-base alloy overlays on superheater tubes has shown significant promise in mitigating potential corrosion issues related to biomass combustion [28–30]. The high Cr content of these material types allows the formation of a slow-growing and protective Cr-rich (Cr_2O_3 or $(Cr_xFe_{1-x})_2O_3$)) oxide scale in mildly corrosive environments [31]. Potassium-induced corrosion on stainless steels and Ni-base alloys has been studied extensively in environments relevant to biomass combustion with a lot of emphasis on the role of KCl and K_2CO_3 [10–19,32–36]. It has been reported that these compounds may react with the protective Cr-rich oxide scale, forming K_2CrO_4:

$$\frac{1}{2}Cr_2O_3(s) + 2KCl(s) + H_2O(g) + \frac{3}{4}O_2(g) \rightleftharpoons K_2CrO_4(s) + 2HCl(g) \quad \text{(R1)}$$

$$\frac{1}{2}Cr_2O_3(s) + K_2CO_3(s) + \frac{3}{4}O_2(g) \rightleftharpoons K_2CrO_4(s) + CO_2(g) \quad \text{(R2)}$$

These reactions result in Cr-depletion of both the oxide and of the alloy substrate. If the alloy at the scale/alloy interface becomes exhausted in Cr, the more noble alloy constituents (e.g., Fe, Ni) start to oxidize forming an oxide which grows rapidly with inferior protective properties. The term "breakaway oxidation" designates the sudden transition from the protective Cr-rich oxide scale to the faster growth Fe,Ni-rich oxide scale. It is usually triggered by a corrosive environment, e.g., "alkaline oxidizing" as in the present case. This paper uses the term "primary protection" to describe the protective properties *before* breakaway while secondary protection denotes the (poorer) protective properties of the scale *after* breakaway as described in previous studies [37].

Due to the presence of HCl, CO_2, and SO_2 in the flue gas of biomass combustion, the most predominant potassium species are usually KCl, K_2CO_3, and K_2SO_4. Consequently, significantly less attention has been paid to KOH-induced corrosion at high temperatures. However, Blomberg et al. argues that KOH(g) may play an important role on fireside corrosion of heat transfer materials in conventional biomass-fired boilers [38–40]. Further studies performed by Blomberg et al. on pure Cr_2O_3 at temperatures between (25–800 °C) report that KOH reacts readily with chromia (Cr_2O_3) already at 200°C, in a similar manner as KCl and K_2CO_3, leading to the formation of K_2CrO_4 (as shown by reaction (R3) [20]:

$$4KOH(s,l,g) + Cr_2O_3(s) + 1\frac{1}{2}O_2(g) \rightleftharpoons 2K_2CrO_4(s) + 2H_2O(l,g) \quad \text{(R3)}$$

The referred study was however carried out on pure chromia, and it is challenging to predict the corrosion effects of potassium chromate formation on chromia forming alloys, such as stainless steel and Ni-base alloys. In these materials, the alloy substrate provides a reservoir of Cr that may diffuse to the corrosion front, replenish the chromia scale, and thereby delaying breakaway corrosion events.

Nevertheless, based on these studies, a sudden slip of alkali-containing compounds from the FR could potentially shift the environment in the AR to become more corrosive than predicted.

Another set of materials studied in environments relevant for superheater applications in biomass combustion are the so-called alumina forming alloys, FeCrAl [41–45]. These materials are usually used in applications at temperatures above 900 °C. At these temperatures, α-Al_2O_3 is formed which exhibits excellent corrosion resistance in mild oxidizing environments [46]. However, at temperatures relevant for conventional superheater applications upon combustion of biomass (~ 400–550 °C) the formation of α-Al_2O_3 is obstructed, leading to the formation of an alumina scale consisting of metastable alumina that reportedly contains relatively high amounts of Cr, making the oxide scale sensitive to breakaway corrosion when in contact with KCl or K_2CO_3 [35,42]. Nevertheless, several studies report good protective properties beyond breakaway for FeCrAl alloys when exposed in environments relevant for superheater application during combustion of biomass [37,47]. Some studies even indicate that the corrosion resistance of FeCrAl alloys is comparable to Ni-based alloys for superheater applications in both biomass and waste-fired boilers, making it an interesting candidate for CLC application [44,45,48]. An approach to further improve the corrosion resistance of FeCrAl alloys has been to incorporate Si into the alloy matrix. Previous research has reported that the addition of 1–2 wt% of Si drastically reduced the corrosion rate of FeCrAl beyond breakaway corrosion in the presence of alkali salts and water vapor [49].

To date, there is no literature describing how the corrosion rate of conventional superheater materials is altered when continuous KOH(g) is introduced in an environment and temperature relevant for the AR in CLC of biomass. Improving the awareness of potential corrosion issues in the AR is crucial for designing commercial CLC units and for finding optimal materials for superheater application. This study aims at investigating the corrosion attack of several materials in two simplified laboratory environments focusing on the AR. One environment mimics a scenario with no alkali slip (referred to as the "clean scenario": 5 % O_2 + 3 % H_2O + N_2 bal.), while the other simulates a scenario with significant alkali release in the AR (referred to as the "alkali slip scenario": 5 % O_2 + 3 % H_2O + N_2 bal. + 16 ppm KOH). The 3 % H_2O simulates humid air used as fluidization medium in the AR and the 5 % O_2 mimics oxygen-depleted air that is expected to exit the AR due to the oxidation of the oxygen carrier. Six materials were investigated and ranged from austenitic stainless steel, Ni-based alloy, and a FeCrAl alloy. The exposures were carried out at 700 °C, corresponding to a material temperature relevant for superheaters in ultra super-critical pressure coal-fired power plants, which represents an important benchmark to reach for combustion of biomass in CLC [50,51]. The 168-h exposure time was chosen to study the initial corrosion attack, which is critical for understanding later-stage corrosion. This duration is common in lab-scale corrosion studies mimicing biomass combustion, enabling us to compare our findings with existing literature and assess how corrosion in the AR of CLC differs from conventional biomass-fired boilers. Chemical and morphological analysis of the corrosion products have been performed to evaluate the exposed materials and to validate their performance.

2. Materials and method

2.1. Sample preparation

The materials investigated in the present study were three austenitic stainless steels (AISI 347H, Sanicro® 25, AISI 310H) and two austenitic Ni-base alloys (Sanicro® 63x59 and Sanicro® 625), all supplied by Alleima AB. Additionally, a ferritic FeCrAl alloy (Kanthal® EF101) provided by Kanthal AB was included. The nominal compositions (wt. %), and the dimensions of the alloy coupons are presented in Table 1.

Prior to exposure, the edges of the coupons were ground with SiC paper P1000 using water as a lubricant. Subsequently, the surfaces of the samples were ground with SiC paper P320 and polished down to 1 μm with a diamond suspension until a mirror-like surface was achieved. The samples were thereafter cleaned with acetone during ultrasonic agitation for 15 min, dried with pressurized air, and stored in a desiccator, using SICAPENT® as desiccant.

2.2. Experimental setup

An illustration of the setup for the corrosion tests is shown in Fig. 2. The exposures were performed using a horizontal tube furnace with a sintered alumina tube (inner diameter: 40 mm). The samples were exposed to a gas composition of 5 % O_2 + 3 % H_2O + N_2 bal. with and without 16 ppm KOH at 700 °C and for a period of 168 h (see Fig. 2a for the setup in the absence of KOH and Fig. 2b for the setup in the presence of 16 ppm KOH). The samples were placed on an alumina sample holder. The gas flow was set to 2.5 cm/s and the flow was controlled using a MesaLabs Bios DryCal Definer 220 calibrator. The humidity of the gas was established by coupling a water bath (set at 24 °C which corresponds to 3 % H_2O by volume) to the gas stream. The water vapor was introduced to the dry gas through a Nafion membrane FC 125–240-5MP from Perma Pure, and the humidity of the gas stream was measured using a Mitchell instruments Optidew Vision™ chilled mirror humidity sensor, prior to entering the horizontal tube furnace.

Continuous KOH(g) in the gas stream was achieved by placing an alumina boat, containing K_2CO_3(s), upstream of the samples at a maximum temperature of 698 °C (see Fig. 2b). At the selected conditions K_2CO_3(s) is expected to react with water vapor forming KOH(g) according to reaction (R4). The equilibrium pressure of KOH(g) in the gas stream was calculated with Factsage 7.3 using FactPS database:

Table 1
Chemical composition of the investigated materials and sample dimensions.

Element (wt.%) Alloy	Fe	Cr	Al	Ni	Mo	Si	Mn	Co	Cu	W	Nb	Minor elements < 0.5 wt%	Dimensions (mm)
Sanicro® 625	4	21.5	–	Bal.	8.7	–	–	–	–	–	3.5	C, P, S, Si, Mn	15x10x2
Sanicro® 63x59	11.1	22.1	–	Bal.	4	–	–	–	–	–	–	C, Al, Si, Ti, Mn	15x10x1
AISI 310H	Bal.	24.5	–	21	–	0.8	1.5	–	–	–	–	C, S	15x10x2
Sanicro® 25	Bal.	22.5	–	25	–	–	0.5	1.5	3	3.6	0.5	C, N, S	15x10x2
AISI 347H	Bal.	17.5	–	11	–	–	1.8	–	–	–	0.7	C, S, Si	20x10x2
Kanthal® EF101	Bal.	12.4	3.7	–	–	1.3	–	–	–	–	–	C, Mn, RE*	15x15x2

*Reactive Element.

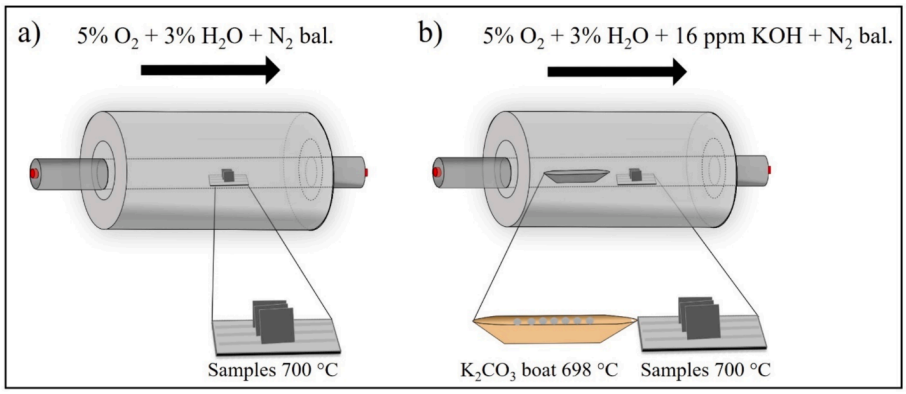

Fig. 2. Illustration of the furnace set-up and exposure conditions. a) exposure without KOH, b) exposure with 16 ppm KOH.

$$K_2CO_3(s) + H_2O(g) \rightleftharpoons 2KOH(g) + CO_2(g)$$
$$p_{eq}(KOH) = 1.64{*}10^{-5} bar\ at\ 698^{\circ}C, 3\%\ H_2O, 420 ppm CO_2 \quad \text{(R4)}$$

The dissociation of $H_2O(g)$ to form $H_2(g)$, a potential corrosive species, is considered negligible. This conclusion is based on thermodynamic calculations using Factsage 7.3 (FactPS database), which shows that the vapor pressure of H_2 is 5.11 x 10^{-12} bar in the present conditions.

By positioning the $K_2CO_3(s)$-containing alumina boat upstream of the samples and at a lower temperature (698 °C), condensation of alkali on the samples (700 °C) was prevented. The temperature of the designated position of the K_2CO_3 containing boat and the samples were measured prior to each exposure. A total of four exposures were carried out for each environment where three alloy types were exposed simultaneously. A total of two exposures for each alloy type were carried out for each environment. The position of the coupons on the alumina sample holder was changed between exposures (i.e., middle and side position) to register possible local effects. The furnace was flushed with 5 % O_2 + 3 % H_2O + N_2 bal. at 900 °C overnight prior to the exposure and the K_2CO_3 boat and samples were first introduced into the furnace as the temperature reached 698 °C and 700 °C, respectively. After exposure, the samples and the K_2CO_3-containing alumina boat were stored in a desiccator, using SICAPENT® as a desiccant. The mass gain of the exposed samples was recorded using a Sartorious™ balance with microgram resolution as soon as they reached room temperature.

2.2.1. Validation test of the experimental setup

To verify the concentration of KOH(g) in the gas stream, the mass of the K_2CO_3 loaded on the alumina boat was recorded before and after each exposure. By correlating the mass change after the exposure together with the temperature, gas flow (1000 ml/min) and using the ideal gas law, the average concentration of KOH(g) was determined to be 16 ± 9 ppm with a maximum value of 25 ppm and a minimum value of 6 ppm. The calculated value is in good agreement with the equilibrium vapor pressure of KOH(g) at 698 °C described in reaction (R4).

To verify potential condensation of alkali at the position of the sample coupons, three gold coupons (15x15x0.3 mm) were exposed at 700 °C in the position normally used for the sample coupons, downstream of the K_2CO_3-containing alumina boat (situated at 698 °C). The selected gas composition was 5 % O_2 + 3 % H_2O + N_2 bal. + 16 ppm KOH and the exposure time was 168 h. The mass change for the gold coupons was recorded to be −0.004, −0.005 and −0.006 mg/cm^2, respectively (Fig. 3). The negligeable mass change suggests that condensation of alkali will not take place at the position of the sample coupons.

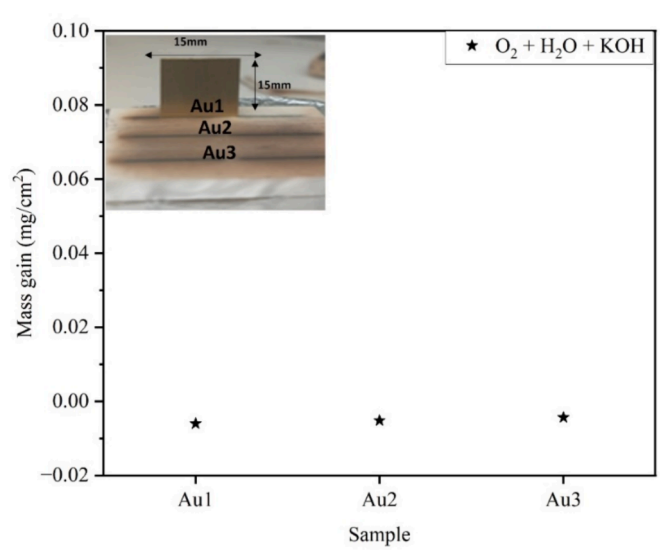

Fig. 3. Image of the gold (Au) sample and mass gains (mg/cm^2) of gold coupons exposed for 168 h in 5 % O_2 + 3 % H_2O + 16 ppm KOH + N_2 bal. at 700 °C.

3. Analysis method

3.1. Scanning electron microscopy, SEM-EDX

Microstructural analyses of the samples after exposure were carried out by scanning electron microscopy (SEM) using an FEI QUANTA ESEM 200 operated in high vacuum mode. The SEM images were conducted using backscattering electrons (BSE) at an accelerated electron voltage ranging between 15–20 keV. Chemical elemental analysis of the samples was carried out by coupling an energy-dispersive X-ray spectroscopy (EDX) detector (Oxford Instruments X-MaxN 80 T) to the SEM instrument. The EDX analysis was carried out at 20 keV, including EDX mapping, point analysis and line scans.

Cross-sections of the exposed samples were prepared by gluing a silica wafer on the surface that was dried overnight. Afterward, the samples were cut in half and polished to a 0.5 μm finish using a Leica EM TXP instrument operated at low speed and without the use of any lubricant. A Leica TIC 3X Broad Ion Beam (BIB) instrument operated at 8.0 kV for 6 h was then utilized to achieve ion-milled cross-sections.

Thickness measurements on the oxide and corrosion product were carried out on the ion-milled cross-sections. SEM images with a vector graphic editor software (INKSCAPE) was used to perform measurements on representative regions. The grain size of the alloy substrate was calculated post exposure. The measurements were carried out on the ion-milled cross sections and derived using SEM combined with the average grain size intersect (AGI) method described in the ASTM E112-13 standard [52]. In this method, a line is drawn within a designated area, and the points where the line intersects with grain boundaries are recorded. Eight lines, with a length of 200 μm, were drawn in total:

$$Grainsize = \frac{\sum \text{Line length}_i}{\sum X_i - 1} \quad (1)$$

3.2. X-ray Diffraction, XRD

The crystalline phases of the corrosion products were analysed with XRD. The XRD analysis was performed with Bragg Brentano configuration on a Siemens Bruker 8 Discovery diffractometer equipped with a Cu source Kα (λ = 1.54178 Å). The measuring range angle was set to $10 < 2\theta < 90°$.

4. Results

4.1. Gravimetric measurements

The mass gain of the materials after 168 h of exposure at 700 °C to 5 % O_2 + 3 % H_2O + N_2 bal. and 5 % O_2 + 3 % H_2O + 16 ppm KOH + N_2 bal. is shown in Fig. 4. Each point, except for AISI 347H which was only measured once due to severe spallation (SI. 1), represents the average mass change of two sample coupons while the error bar indicates the spread. In absence of KOH(g), the mass gain was small (<0.1 mg/cm^2) for all materials except for AISI 347H (4.5 mg/cm^2) (Fig. 4). As AISI 347H experienced severe spallation, the exposed sample was separated from the other samples directly after removing it from the furnace and put in a pre-weighed sample holder in order to collect any spalled oxide and achieve an accurate gravimetrical reading.

Exposure in the presence of KOH(g) resulted in a significant mass gain for all materials except for Kanthal® EF101. AISI 347H underwent severe spallation during cooling similar to what was described above. By collecting the spalled oxide, the mass gain was measured to 5.89 mg/cm^2, which was the highest mass gain of all investigated samples. The stainless steels Sanicro® 25 and AISI 310H obtained a mass gain of 3.31 mg/cm^2 and 2.44 mg/cm^2, respectively, which was about 55 times greater compared to corresponding exposure in the absence of KOH(g).

An increase in mass gains was recorded for the Ni-base alloys in the presence of KOH(g). It may be noted that the difference between Sanicro® 625 and AISI 310H was minor (2.37 mg/cm^2 vs 2.44 mg/cm^2, respectively). The mass gains of Sanicro® 625 and Sanicro® 63x59, were about 75–90 times greater in the presence of KOH compared to when KOH was absent.

The mass gain recorded in the presence of KOH(g) (0.098 mg/cm^2) was roughly 10 times higher compared to that in absence of KOH(g) (0.01 mg/cm^2) for the FeCrAl alloy Kanthal® EF101.

4.2. Microstructural analysis

To facilitate the interpretation of the microstructural analysis, key results are summarized and presented in Table 2. Corrosion products which contains additional elements from the environment i.e. potassium ($KFeO_2$, K_2CrO_4, $K_2(Cr,Mo)O_4$, K-aluminate), are categorized separately and defined as "other corrosion products" in the table.

4.2.1. Stainless steels (AISI 347H, Sanicro® 25 and AISI 310H)

Fig. 5 shows SEM cross-sections of the stainless steels exposed to O_2 + H_2O and O_2 + H_2O + KOH.

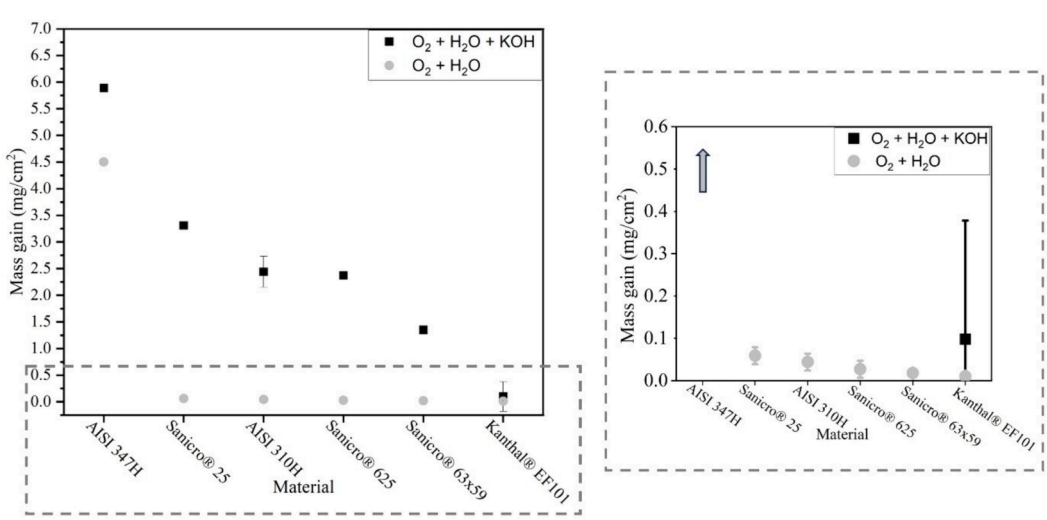

Fig. 4. Mass gain, expressed as mg/cm^2 of the different materials exposed for 168 h at 700 °C in 5 % O_2 + 3 % H_2O + N_2 bal. and 5 % O_2 + 3 % H_2O + 16 ppm KOH + N_2 bal.

Table 2
Summary of the microstructural analysis for each exposure.

5 % O_2 + 3 % H_2O + N_2 bal.						
Material **Analysis**	**AISI 347H**	**Sanicro® 25**	**AISI 310H**	**Sanicro® 625**	**Sanicro® 63x59**	**Kanthal® EF101**
Alloy grain size (μm)	35	25	51	13	21	17
Outward-growing oxide (μm)	Traces (spallation)	0.2–1.3	0.2–0.5	0.2	0.2	0.05
Composition	Fe-rich oxide	Cr-rich oxide, Fe-rich oxide	Cr-rich oxide, Fe-rich oxide	Cr-rich oxide	Cr-rich oxide	Al-rich oxide
Inward-growing oxide (μm)	Traces (spallation)	0.1–0.5	*	–	–	–
Composition	Fe-Cr oxide	Fe-Cr-Ni oxide	*	–	–	–
Internal oxidation zone (μm)	20–40	–	–	–	–	–
Other corrosion products	–	–	–	–	–	–
Breakaway corrosion	Yes	Yes (local)	Yes (local)	No	No	No

* Not detected with EDX or XRD.

5% O_2 + 3% H_2O + 16 ppm KOH + N_2 bal.						
Material **Analysis**	**AISI 347H**	**Sanicro® 25**	**AISI 310H**	**Sanicro® 625**	**Sanicro® 63x59**	**Kanthal® EF101**
Alloy grain size (μm)	39	22	43	17	19	15
Outward-growing oxide (μm)	Traces (spallation)	1–8	4–6	3–6	1–2	0.06
Composition	Fe-rich oxide	Fe-rich oxide, CuO	Fe-rich oxide	Ni-rich oxide	Ni-rich oxide	Al-rich oxide
Inward-growing oxide (μm)	Traces (spallation)	1–6	2–5	1–5	0.5–1	–
Composition	Fe-Cr oxide	Fe-Cr-Ni oxide	Fe-Cr-Ni oxide	Cr-rich oxide	Cr-rich oxide	–
Internal oxidation zone (μm)	20–50	1–20	1–2	1–13	1–2	–
Other corrosion products	$KFeO_2$	$KFeO_2$, K_2CrO_4	$KFeO_2$, K_2CrO_4	$KFeO_2$, $K_2(Cr,Mo)O_4$	K_2CrO_4	Potassium Aluminate**
Breakaway corrosion	Yes	Yes	Yes	Yes	Yes	No

** Indicated with SEM/EDX. not detected with XRD.

Typical features of Alloy AISI 347H observed after exposure to O_2 + H_2O included severe internal oxidation together with the formation of a multilayer oxide scale (Fig. 5a). The boxed area of Fig. 5a is shown in detail in Fig. 6. From SEM-EDX line scan it is shown that on top of the alloy substrate, remaining traces of a 2–3 μm outward-growing Fe-rich oxide were observed (region III in Fig. 6c). The thickness should be discussed with caution due to the severe spallation of the oxide scale observed during the cooling process post exposure (see supplementary information, SI. 1a). Beneath, a roughly 2 μm inward-growing (Fe,Cr) oxide (region II in Fig. 6c) was present on top of a 20–40 μm continuous internal oxidation zone (IOZ) (region I in Fig. 6c). The IOZ typically comprised of two regions; oxide particles enriched in Cr and Fe (darker regions) and metal surface enriched in Ni (bright region) (Fig. 6b). The number density of oxide particles was greater closer to the IOZ/oxide interface. The alteration between the oxide regions and metal substrate was further confirmed by the SEM-EDX line where a reduced oxygen content was observed overall in this region, indicating a region of not fully oxidized alloy substrate. The corrosion morphology was similar in the presence of KOH(g), namely the formation of a roughly 20–50 μm thick IOZ zone on top of a multilayer oxide scale with indications of severe spallation of the oxide scale (Fig. 5b & SI. 1b). The biggest difference of the IOZ between the two different environments was that the Fe,Cr oxide precipitates increased in numbers and appeared in a more continuous fashion in presence of KOH (Fig. 5b). In addition, XRD analysis (SI. 2) confirmed the formation of $KFeO_2$ in presence of KOH(g).

Sanicro® 25 and AISI 310H formed well-adherent oxide scales when exposed to O_2 + H_2O, where the oxide thickness was about 0.2–1.3 μm and 0.2–0.5 μm, respectively (Fig. 5c and Fig. 5e). Clear signs of Fe-rich oxide nodules covering the surface of AISI 310H and Sanicro® 25 were observed during plan-view SEM analysis (top corner of Fig. 5e & SI. 3) which is a strong indicator that the oxide has entered the secondary protective regime, i.e. local breakaway corrosion has transpired [53,54].

The presence of KOH(g) significantly accelerated the corrosion rate of Sanicro® 25 (Fig. 5d). The scale morphology was characterized by heterogenous patch-like features with multiple layers. The localized nature of corrosion could be coupled to the alloy microstructure, where a thicker oxide scale was observed at the center of the alloy grains while a thinner oxide scale covered the alloy grain boundaries. Fig. 7 shows the SEM-EDX analysis of the highlighted region in Fig. 5d. The top layer of the scale consisted of a CuO layer of about 1 μm thickness followed by 3–13 μm thick layer of potassium ferrate ($KFeO_2$). Albeit not present on the SEM image, indication of K_2CrO_4 formation was detected with XRD (SI. 2). Beneath the $KFeO_2$ layer, an Fe-rich outward-growing oxide with a thickness ranging from 1-8 μm was present and consisted of 70 % Fe, 26 % Ni and traces of Cr (2 %) and K (2 %) (cationic %). Below, a continuous inward-growing Cr-rich $(Fe,Cr,Ni)_3O_4$ spinel oxide (based on SEM-EDX analysis) was present with the average composition of 22 % Fe, 64 % Cr and 14 % Ni (cationic %) and with a thickness of 1–6 μm. Discontinuous internal oxidation zones (IOZ) were detected beneath the oxide scale. The IOZ exhibited similar features as in the case of AISI 347H, namely unreacted metal substrate with high Ni content (bright regions) and Fe,Cr-rich oxide (dark region). The IOZ was more extensive in areas suffering from severe corrosion and ranged from 1-20 μm in thickness.

Fig. 8 shows the SEM cross-section image and the corresponding EDX maps of the highlighted region in Fig. 5f of AISI 310H exposed to O_2 + H_2O + KOH. The top of the scale consisted of K_2CrO_4, ranging from 1-4 μm in thickness, followed by a layer of $KFeO_2$, with a thickness of 1–2 μm. Similar to Sanicro® 25 and AISI 347H, a multilayer oxide scale was present, consisting of a roughly 4–6 μm thick outward-growing Fe-rich oxide with a composition of 83 % Fe, 10 % Ni, 3 % Cr and 4 % K (cationic %). Below, an inward-growing oxide was recognized as a Cr-rich $(Fe, Cr, Ni)_3O_4$ spinel containing 63 % Cr, 22 % Fe and 15 % Ni (cationic %), with a typical thickness of 2–5 μm. Moreover, Ni-enrichments of the alloy substrate were observed at the corrosion front, i.e., just beneath the inward-growing oxide scale. EDX analysis revealed the formation of a discontinuous and thin IOZ at the corrosion front, with similar features as described before (see high magnification SEM image in Fig. 8). However, it should be noted that the occurrence of IOZ was significantly less compared to Sanicro® 25.

4.2.2. Ni-base alloys (Sanicro® 63x59 and Sanicro® 625)

The Ni-base alloys Sanicro® 63x59 and Sanicro® 625 formed a thin (0.2 μm), adherent, and homogenous oxide scale after 168 h of exposure to O_2 + H_2O (Fig. 9a, c). SEM/EDX analysis (see SI. 4) revealed that both alloys formed a Cr-rich oxide scale on the surface, likely Cr_2O_3.

The two alloys experienced accelerated corrosion when exposed to O_2 + H_2O + KOH(g) (see Fig. 9b and d). Fig. 10 shows the SEM image and the corresponding EDX line scan of the highlighted region in Fig. 9b of Sanicro® 625. Several corrosion product layers could be

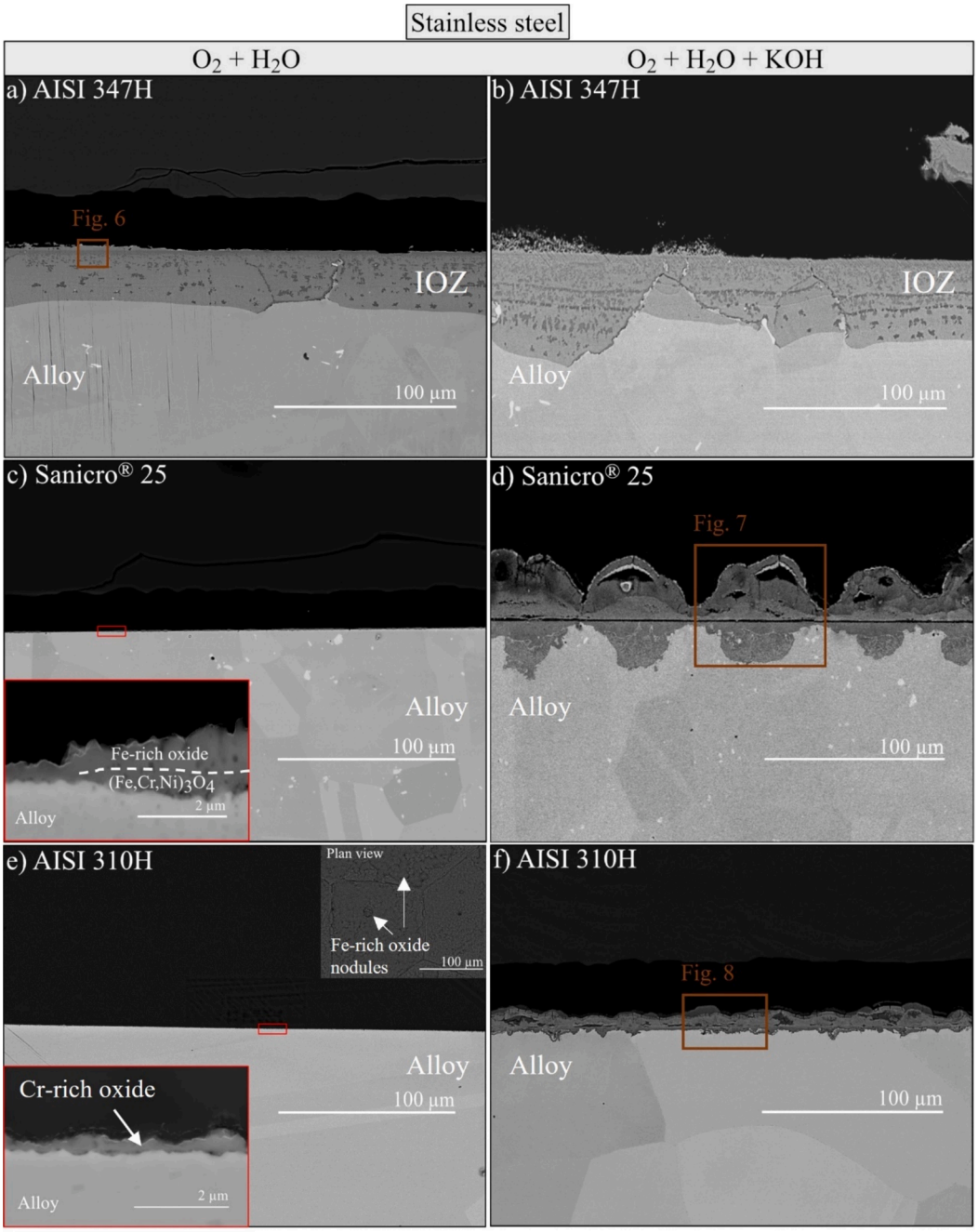

Fig. 5. SEM cross-section micrographs of the stainless steels exposed for 168 h at 700 °C in 5 % O_2 + 3 % H_2O + N_2 bal. and 5 % O_2 + 3 % H_2O + 16 ppm KOH + N_2 bal.

distinguished. On top, a 2–7 µm thick layer with a chemical composition of 66 % K, 17 % Cr, and 17 % Mo (cationic %), was detected with EDX. The elemental composition suggests the formation of $K_2(Cr,Mo)O_4$. Below, an approximately 3–5 µm thick oxide scale consisting predominately of Ni, 90 % Ni, 10 % Fe (cationic %), was identified. Furthermore, an inward-growing oxide varying from 1-5 µm in thickness and enriched in Ni and Cr was present. A discontinuous IOZ, ranging from 1-13 µm in thickness, was present beneath the inward-growing oxide layer. The IOZ's were comprised of Cr-rich oxide precipitates (darker regions) and remaining metal enriched in Ni (brighter regions).

Fig. 11 shows the SEM cross-section images and the corresponding EDX line scan of the highlighted region in Fig. 9d of Sanicro® 63x59 exposed to KOH(g). The micrograph reveals the formation of a homogenous and less corroded surface compared to the stainless steels and Sanicro® 625, which aligns well with the gravimetric analysis presented in Fig. 4. The corrosion product, consisted of a roughly 3–7 µm thick K_2CrO_4 layer growing on top of a 1–2 µm thick Ni-rich oxide scale consisting of about 64 % Ni, 20 % Fe, 9 % Cr, 2 % Mo and 5 % K (cationic %) (Fig. 11). Indication of an inward-growing Cr-rich oxide scale is shown in the presented EDX maps. However, the oxide scale was < 1 µm making it challenging to confirm its composition with the current set-up. Traces of IOZ were observed across the cross-section, although less pronounced compared to Sanicro® 25 and Sanicro® 625. Lastly, void formations, depleted in Cr, alongside the grain boundaries of the alloy, were present at the metal/oxide interface (see Fig. 10).

4.2.3. FeCrAl alloy (Kanthal® EF101)

Fig. 12 shows the SEM cross-section images and corresponding EDX

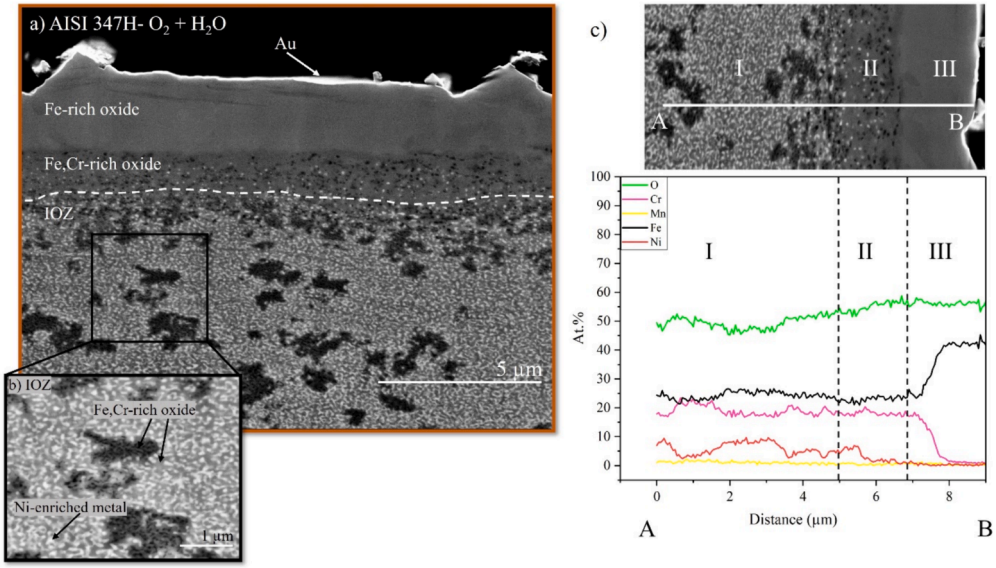

Fig. 6. A) sem cross-section micrograph of aisi 347h exposed at 700 °C in 5 % O_2 + 3 % H_2O + N_2 bal. Only traces of fully oxidized Fe-rich and Fe,Cr-rich regions were observed on the surface due to severe spallation. Below, a continuous IOZ was present. b) The IOZ can be divided into two regions that consist of Fe,Cr-rich oxide (dark region) alongside Ni-enriched metal (bright region). c) EDX line scan of selected region in (a).

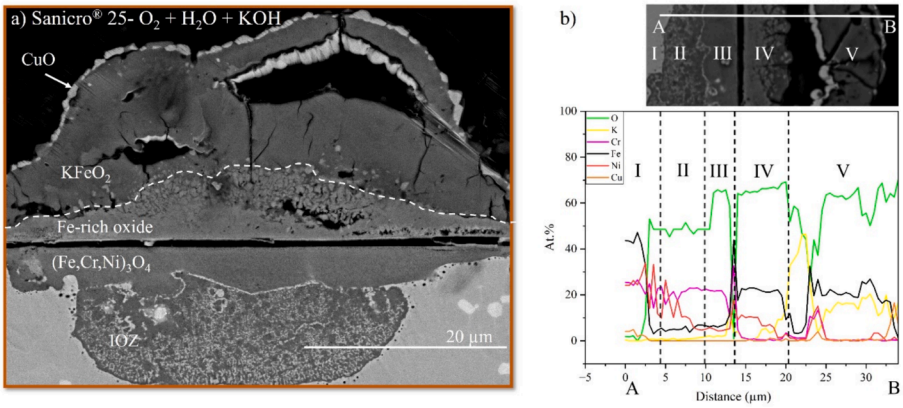

Fig. 7. A) sem cross-section micrograph of sanicro® 25 exposed for 168 h at 700 °C in 5 % O_2 + 3 % H_2O + 16 ppm KOH + N_2 bal. b) EDX line scan of representative region.

maps of Kanthal® EF101 exposed in O_2 + H_2O and O_2 + H_2O + KOH. From SEM-EDX analysis it is suggested that a 0.05 µm Al-rich oxide scale had formed on top of the alloy substrate with no signs of spallation or crack formation in the presence of O_2 and H_2O. When exposed to KOH (g), a roughly 0.3 µm corrosion layer containing K, Al, and O was identified. The increased intensity of Al from the SEM-EDX map analysis observed on top of the alloy substrate indicates the formation of a roughly 0.06 µm oxide scale enriched in Al (see Fig. 12b). However, the exact composition of the oxide scales and corrosion products presented should be interpreted cautiously owing to the insufficient resolution of the SEM-EDX analysis. Nevertheless, no signs of severe corrosion were observed on this alloy regardless of environment, which is consistent with the gravimetric analysis presented in Fig. 4.

5. Discussion

5.1. Clean scenario (O_2 + H_2O + N_2)

Ideally, there should be minimal transport of volatile alkali from the FR to the AR in CLC of biomass. When simulating such a scenario in the present study (5 % O_2 + 3 % H_2O + N_2 bal.), all chromia formers except 347H, (i.e., the stainless steels and the Ni-base alloys), showed protective behavior, a thin adherent oxide scale being present (<0.5 µm) after 168 h at 700 °C (Figs. 5 and 9).

The microstructural analysis revealed that the Ni-base base alloys retained a primary protective chromium-rich oxide scale while all the stainless steels had transitioned to the secondary protective regime, albeit to a different degree (Figs. 5 and 9). Stainless steels are known to suffer from breakaway corrosion in presence of water vapor at temperatures and conditions relevant for this study (600–900 °C) [55–59]. This has been attributed to the formation of chromic acid ($CrO_2(OH)_2$ (g)) according to the following reaction:

$$Cr_2O_3(s) + 2H_2O(g) + 1\frac{1}{2}O_2(g) \rightleftharpoons 2CrO_2(OH)_2(g) \quad \text{(R5)}$$

The evaporation of Cr is argued to trigger breakaway corrosion, i.e., breakdown of the primary protective oxide layer and the formation of a multilayer oxide scale consisting of an outward-growing Fe-rich oxide layer scale and an inward-growing (Fe,Cr,Ni) spinel with inferior protective properties [57]. Local breakaway corrosion was observed on Sanicro® 25 and 310H in the present study, with similar corrosion morphology as reported in previous studies related to Cr-evaporation

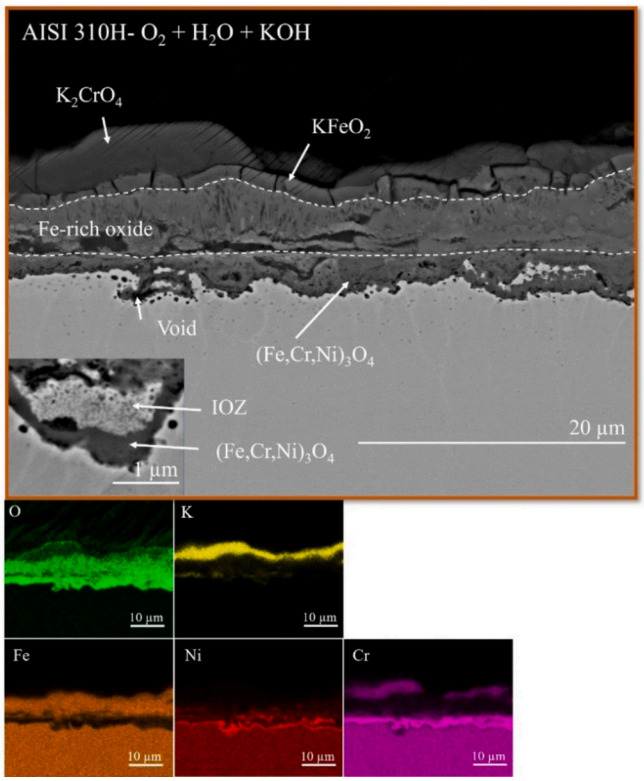

Fig. 8. SEM cross-section micrograph and corresponding EDX maps of AISI 310H exposed for 168 h at 700 °C in 5 % O_2 + 3 % H_2O + 16 ppm KOH + N_2 bal.

[43–47]. Although local breakaway corrosion occurred, the overall appearance of the oxide scale remained thin and adhered to the substrate.

Severe corrosion was observed in the clean scenario of alloy 347H. Previous studies have correlated the resistance to breakaway corrosion by Cr-evaporation with the Cr/Fe ratio in stainless steels [55]. A higher Cr/Fe ratio enhances the chromium supply to the corrosion front, leading to improved resistance of the Cr-rich oxide scale. As shown in Table 1, 347H has a significantly lower chromium content compared to the other chromia-forming alloys, i.e., stainless steels, and Ni-base alloys, examined in this study. This lower chromium content may be associated with the severe corrosion observed. Furthermore, severe spallation was observed during cooling regardless of the environment for 347H (Fig. 5a and b). It is widely acknowledged that during cooling, the mismatch of the coefficient of thermal expansion (CTE) between the oxide scale and the alloy together with the interfacial shear stresses generated during oxide growth may cause delamination and spallation of oxide scales [31,60]. For instance, Liu et al. quantified the maximum shear stress observed at the oxide/substrate interface as a function of oxide scale thickness for stainless steel at 850 °C [61]. A strong correlation was found, where the interfacial stresses increased with the thickness of the oxide scale. This is in good agreement with the results from this study, where spallation was only observed for AISI 347H. The microstructural analysis showed that AISI 347H underwent severe corrosion forming a roughly 35–40 µm IOZ and an Fe-rich oxide scale, after 168 h of exposure in the absence of KOH(g). Given the thickness of the IOZ and present Fe-rich oxide scale together with the mass gain recorded, it is argued that the outward growing oxide scale is orders of magnitude thicker than for the other tested alloys. It is argued that the severe spallation is caused by stresses at the oxide/IOZ interface. The adhesion of the oxide scale will be a critical parameter for corrosion resistance of superheater tubes in the AR. If the material undergoes spallation upon thermic cycling, fresh metal surface will be exposed leading to rapid corrosion. Thus, given the significant corrosion and scale spallation observed in this relatively mild corrosive environment, AISI 347H is likely unsuitable for superheater application in the AR side of a CLC unit.

While AISI 347H suffered extensive corrosion and scaling in the absence of KOH(g), the other two stainless steels (Sanicro® 25 and AISI 310H) showed essentially protective behavior, exhibiting only local breakaway corrosion (Figs. 4 and 6). This difference is attributed to the higher concentrations of Cr and Ni in Sanicro® 25 and AISI 310H (Table 1). Furthermore, Persdotter et al. have shown that the protective properties of oxide scales on Fe-based alloys *beyond* breakaway, i.e., after the transition to the secondary protective regime, can be improved by higher concentrations of Ni and Cr in the alloy [37]. The observation that Sanicro® 25 and 310H suffer local breakaway corrosion while Sanicro® 63x59 and Sanicro® 625 do not, is in accordance with e.g., Pettersson et al. who reported that an increased Ni content of Fe-Cr-Ni alloys improved the protective properties of the primary oxide scale, i.e., *before* breakaway corrosion, in a humid environment at 600–800 °C [62,63].

FeCrAl alloys are well-known for their superior resistance towards corrosion at high temperatures (>900 °C) due to their ability to form a highly protective α-Al_2O_3 scale [46,64]. This study shows that Kanthal® EF101 forms an oxide layer with excellent protective properties in O_2 + H_2O + N_2 already at 700 °C, the corrosion rate being minimal with no signs of breakaway corrosion. Microstructural analysis revealed the presence of a roughly 0.05 µm, adherent, Al-rich oxide scale, with low amounts of Cr and Fe (see Fig. 12a). Chromium is known to be important for the ability of alumina-forming high temperature alloys to form protective alumina scales, in what is commonly referred to as the third element effect [31]. However, chromia volatilization is unlikely to play a role in corrosion of Kanthal® EF101 because of the rapid formation of an alumina-rich surface layer. This is supported by Reddy et al. and Sand et al. who reported negligible or very little Cr-evaporation from Kanthal® EF101, respectively, (denominated A197 in the studies referred to) between 600–800 °C in air containing 3–40 vol% H_2O [58,65].

5.2. Alkali-slip scenario (O_2 + H_2O + KOH)

The improved steam data anticipated for biomass-fired CLC power boilers compared to conventional biomass-fired boilers relies on the assumption that the AR facilitates a mild corrosive environment, i.e., minimal transport and release of corrosive species from the FR to the AR. However, previous studies have detected volatile alkali release in the AR, likely in the form of KOH(g), suggesting that alkali may be transferred from the FR to the AR during biomass combustion in CLC [25]. Thus, it is crucial to investigate how such events may affect the corrosion rate of superheaters installed in connection to the AR. In the alkali slip scenario, 16 ppm of KOH(g) was added to the gas atmosphere in the laboratory exposures in order to mimic a situation where alkali is continuously transferred from the FR to the AR and subsequently released as KOH(g).

It is well-known that the presence of certain alkali compounds, e.g., KCl and K_2CO_3, in an oxidizing environment, can convert chromia in the protective scale on high-temperature alloys to potassium chromate (K_2CrO_4), leading to a drastic increase of corrosion (see reactions (R1-2)). Thus, the formation of chromate, e.g., K_2CrO_4, is reported to be accompanied by the appearance of a multilayer oxide scale with inferior protective properties, [12,14,19–22,58]. This is in line with the present study which demonstrates that the addition of KOH(g) to a gas containing O_2 and H_2O greatly accelerates the corrosion of the chromia-forming alloys, Sanicro® 25, AISI 310H, Sanicro® 63x59 and Sanicro® 625. Indeed, it is suggested that the corrosion of chromia-forming alloys in O_2 + H_2O + KOH(g) environment is caused by reaction (R3). Based on the oxide thickness measurements, the alloys can be ranked according to their ability to withstand corrosion in O_2 + H_2O + KOH(g) environment: AISI 347H < Sanicro® 25 < AISI 310H < Sanicro® 625 <

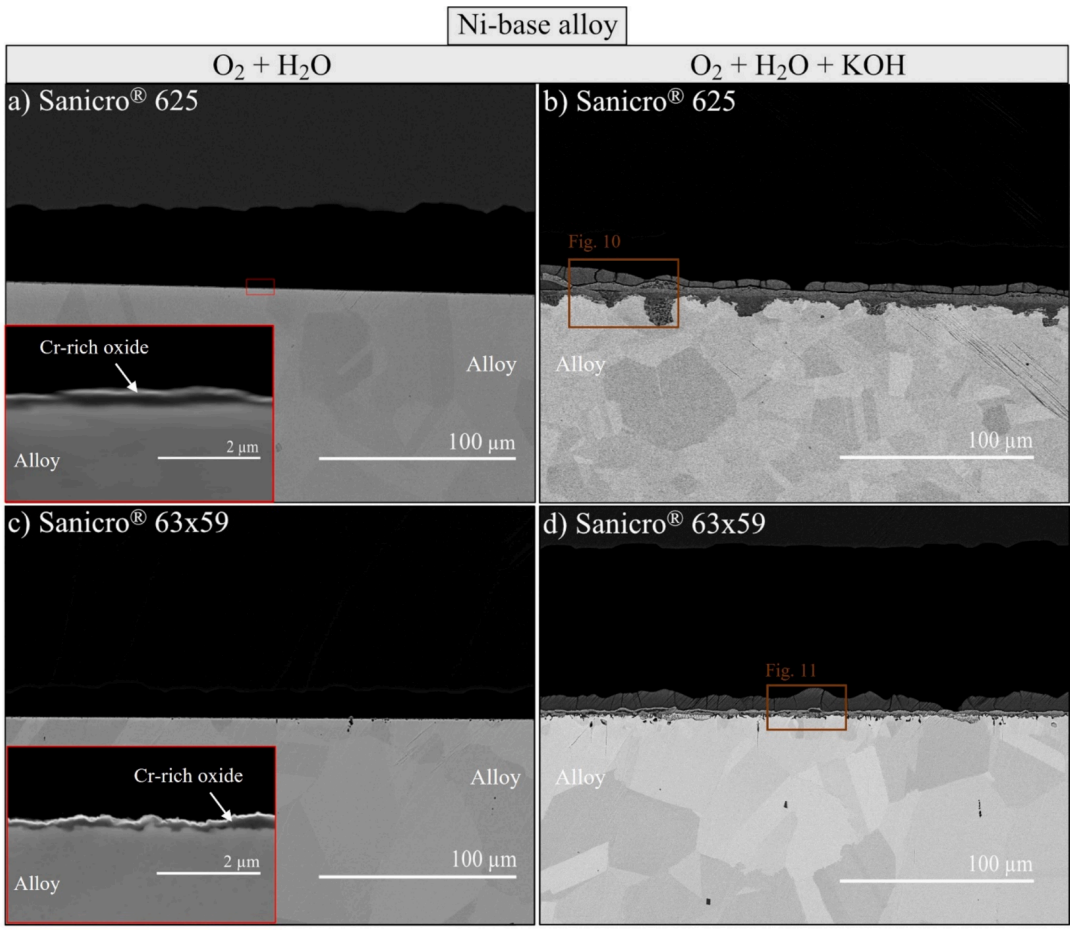

Fig. 9. SEM cross-section micrographs of the Ni-base alloys exposed for 168 h at 700 °C in 5 % O_2 + 3 % H_2O + N_2 bal. and 5 % O_2 + 3 % H_2O + 16 ppm KOH + N_2 bal.

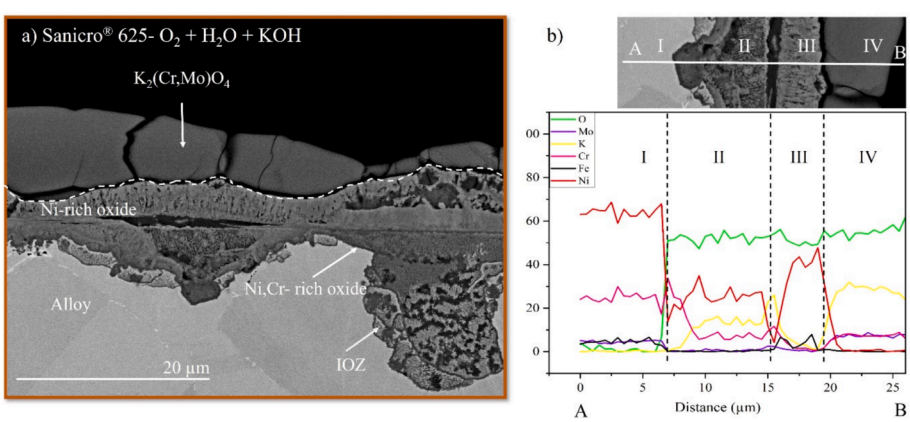

Fig. 10. A) sem cross-section micrograph of sanicro® 625 exposed for 168 h at 700 °C in 5 % O_2 + 3 % H_2O + 16 ppm KOH + N_2 bal. b) EDX line scan of selective region in (a).

Sanicro® 63x59.

The micrographs of the austenitic stainless steels Sanicro® 25 and AISI 310H revealed that the whole surface has suffered breakaway corrosion. As such, the experimental conditions are forceful enough to trigger breakaway corrosion according to reaction (R3). Both alloys feature oxide scales with an outward-growing Fe-rich oxide scale and an inward-growing Cr-rich $(Fe,Cr,Ni)_3O_4$ spinel (Figs. 7-8), in good agreement with previous studies on breakaway corrosion of austenitic stainless steels in the presence of alkali [36,66–68]. As shown in Fig. 8, Sanicro® 25 exhibited heterogenous corrosion, with the most severe corrosion affecting the center of the alloy grains. Such a dependence of corrosion on alloy grain structure is common in austenitic stainless steels and it is often attributed to the dominance of grain boundary diffusion in the transport of chromium to the growing chromia scale in the studied temperature range [38,49]. Thus, depletion of Cr in the oxide scale by the formation of K_2CrO_3 will be replenished more quickly at the grain boundaries, likely resulting in an incubation period before breakaway corrosion is triggered. Another interesting phenomenon observed on

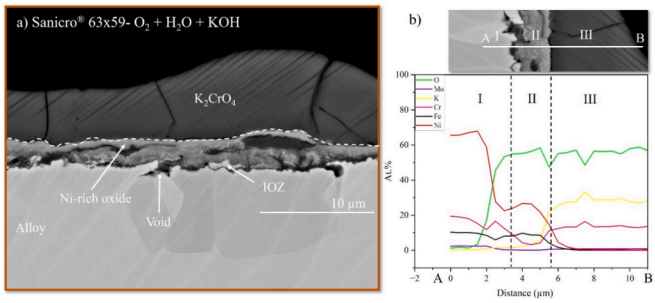

Fig. 11. A) sem cross-section micrograph of sanicro® 63x59 exposed for 168 h at 700 °C in 5 % O_2 + 3 % H_2O + 16 ppm KOH + N_2 bal. b) EDX line scan of selected region in (a).

Sanicro® 25 is the accumulation of Cu-rich oxide at the gas/scale interface. This is noteworthy because Cu has a significantly lower affinity for oxygen compared to alloy elements like Fe and Cr. Therefore, the presence of Cu-rich oxide at the scale/gas interface is surprising, as it indicates an initial preferred oxidation of Cu. Similar features have been observed by Intiso et al. upon studying the corrosive behavior of Sanicro® 25 in dry and wet conditions at 600 °C [57]. They concluded that it is possible that enriched Cu-precipitates initially form at the metal/oxide interface upon oxidation of the more reactive elements such as Fe and Cr. Over time the Cu-rich precipitates may lose their contact with the alloy substrate and migrate through the oxide scale as Cu-ions and eventually oxidize to the Cu^{2+} state at the oxide/gas interface, similar to what was observed in the present study.

Because of the larger grains in AISI 310H compared to Sanicro® 25, one might expect more uneven corrosion in the former case. Instead, corrosion was more evenly distributed over the surface of AISI 310H, with no obvious relation to alloy microstructure (Fig. 5d and 5f). This shows that the differences in scale morphology cannot be explained solely by chromium diffusion in the alloy but could also be influenced by the concentration of important alloy elements such as Cr. Similarly, Persdotter et al. reported no correlation between corrosion rate and alloy grain size in K_2CO_3-induced corrosion of various austenitic stainless steels at 600 °C [37].

The presence of KOH(g) promoted internal oxidation both of the austenitic stainless steels (Sanicro® 25 and AISI 310H) and on the Ni-base alloys (Sanicro® 625 and Sanicro® 63x59). The internal oxidation zone (IOZ) consisted of a mixture of two phases: Cr,Fe-rich oxide (for stainless steels), or Cr-rich oxide (for Ni-base alloys) and Ni-rich remaining alloy. Thermodynamic calculations carried out by Jonsson et al. and Col et al. link this phenomenon to the equilibrium composition of the spinel as a function of partial pressure of oxygen. At low partial pressure of oxygen, Ni is prohibited from entering the Fe,Cr spinel thus leaving behind a Ni-enriched alloy substrate [68,69]. Considering the low concentration of Fe in Ni-base alloys, Cr-rich internal oxidation zones has been observed on Ni-base alloys in the presence of alkali in previous studies, similar to what is presented in the present study [36,70]. Internal oxidation is a dynamic process where the local composition of the surrounding alloy and oxygen activity may alter as corrosion progresses. These alterations may facilitate phase transitions of the internal oxide zones over time leading to the formation of either a poor protective oxide or a protective oxide, also known as a healing layer [69]. As such, it is important to consider long-term exposure tests to enhance our comprehension of how the formation IOZ may impact the corrosion rate over extended periods in this environment.

$KFeO_2$ was identified on the stainless steels AISI 310H, and Sanicro® 25 upon exposure to KOH(g) (Figs. 7 and 8). Hematite (Fe_2O_3) has been reported to react with KOH to form $KFeO_2$ [20]:

$$Fe_2O_3(s) + 2KOH(s,l,g) \rightleftharpoons 2KFeO_2(s) + H_2O(g) \quad \text{(R6)}$$

As Fe-rich oxide was observed on the surface beyond breakaway corrosion on both Sanicro® 25 and 310H, it is also argued that the following reaction may occur in an oxidizing environment:

$$Fe_3O_4(s) + 3KOH(g) + \frac{1}{4}O_2(g) \rightleftharpoons 3KFeO_2(s) + \frac{3}{2}H_2O(g) \qquad \Delta G^0_{700^\circ C} = -309 kJ/mol \quad \text{(R7)}$$

As such, we suggest that K_2CrO_4 forms initially according to reaction (R3) for Sanicro® 25 and 310H in presence of KOH, leading to the breakdown of the primary protective oxide. This allows rapid formation

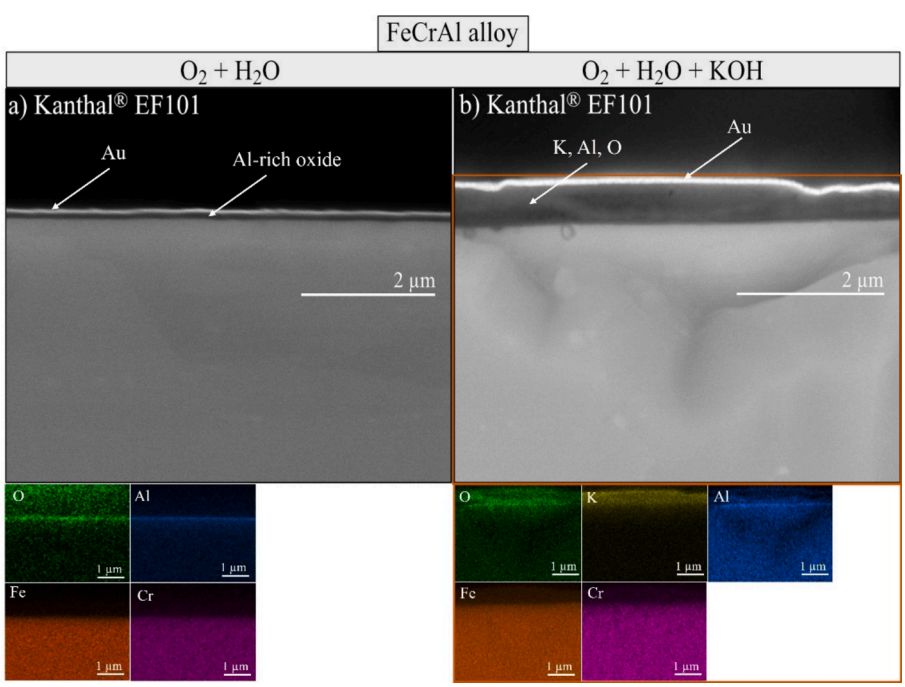

Fig. 12. SEM cross-section micrographs and corresponding EDX maps of Kanthal® EF101 exposed for 168 h at 700 °C in a) 5 % O_2 + 3 % H_2O + N_2 bal. and b) 5 % O_2 + 3 % H_2O + 16 ppm KOH + N_2 bal..

of Fe-rich oxide scale which subsequently may react with KOH(g) leading to the formation of $KFeO_2$ according to reaction (R6) or (R7). Thus, it is suggested that KOH(g) interacts with both the primary *and* the secondary protective oxide scale. While its effect on the corrosion rate through the disruption of the primary Cr-rich oxide scale is apparent, further studies are needed to better comprehend the influence of KOH(g) and the formation of $KFeO_2$ beyond breakaway corrosion.

It is evident that the two Ni-base alloys tested cannot retain the primary protective Cr-rich oxide scale when exposed to KOH(g) (see Fig. 9). Large amounts of K_2CrO_4 were detected on Sanicro® 63x59 suggesting that breakaway corrosion has been triggered by reaction (R3). In the case of Sanicro® 625, a solid solution of potassium chromate and potassium molybdate, $K_2(Cr, Mo)O_4$, was detected rather than potassium chromate. Molybdenum containing corrosion products are rarely reported on high temperature alloys, elemental molybdenum usually accumulating in the alloy substrate, beneath the oxide scale. It is suggested that the occurrence of molybdate in this case is connected to the highly alkaline experimental conditions which are known to stabilize molybdate and to the high concentration of Mo in the alloy. Mo alloying has been associated with both enhancing and reducing the corrosion protective properties of Ni-base alloys [71]. In a systematic investigation of the influence of Mo on corrosion of Ni-base chromia-forming model alloys, Izzuddin et al. reported that the corrosion resistance in the presence of alkali chloride vapor and O_2 at 570 °C, was optimal at an Mo concentration of 3 wt% [71]. The beneficial effects of Mo were attributed to its ability to promote the formation of an outward-growing Ni-rich oxide that hindered chromate formation, thus preventing Cr depletion of the alloy substrate. However, the present study clearly shows that K_2CrO_4 is formed, suggesting that the initial oxide is Cr-rich. This is in accordance with the observation of a Cr-rich oxide layer seen for the Ni-base alloys in the absence of KOH(g) (Fig. 8). Nevertheless, the formation of Ni-rich oxide scale beyond breakaway corrosion has been reported in many cases to reduce depletion of Cr via Cr-evaporation. Considering that there was no indication in the present study that the Ni-rich oxide scale further reacted with KOH(g) it is reasonable to argue that the Ni-rich oxide scale may also work as a protective barrier for Cr depletion via chromate formation thus reducing depletion of Cr from the alloy substrate.

An interesting feature observed on Sanicro® 63x59 was the formation of voids at the corrosion front when exposed to KOH. These were particularly severe at the grain boundaries and were enriched in Ni (Fig. 9). Void formation has been documented in prior studies on Ni-based alloys, with the phenomenon often attributed to the different diffusion coefficients of Cr and Ni. This results in the accumulation of vacancies in the Ni-enriched region leading to void formation, known as the Kirkendall effect. Work reported by Ssenteza et al. has shown that these voids can progress over time and is suggested to reduce the adhesive properties of the oxide scale on Ni-base alloys [47].

Lastly, while this study demonstrates that KOH(g) significantly accelerated the corrosion rate of both stainless steels and Ni-base alloys, the same effect was not recognized for the FeCrAl alloy Kanthal® EF101 (Fig. 11b). The oxide scale is suggested to consist of a roughly 0.06 μm Al-rich oxide, similar to what was detected in absence of KOH. Furthermore, no signs of K_2CrO_4 or $KFeO_2$ on top of the oxide scale were observed. These results further support what was discussed in section 5.1, namely that a predominantly pure Al-rich oxide scale forms on top of the alloy in these environments. Consequently, accelerated corrosion related to Cr-evaporation, reaction (R5) or Cr-depletion by KOH(g), reaction (R3) is argued to be negligible. Previous studies have shown that the ability of FeCrAl alloys to form a pure Al_2O_3 is highly dependent on the exposure temperature [72,73]. For example, Josefsson et al. demonstrated that the concentration of Fe and Cr in an Al_2O_3 oxide scale is lower at 700 °C compared to 500 °C and 600 °C when exposed to dry air [73]. Furthermore, the addition of Si to FeCrAl alloys has also been shown to promote the formation of an Al-rich oxide scale, even at temperatures as low as 600 °C [42,49]. In a recent study, Eklund et al. demonstrated that the addition of 2 wt% Si on a FeCrAl alloy prevented the occurrence of breakaway corrosion when exposed for 2000 h to K_2CO_3 in 5 % O_2 and 95 % N_2 at 600 °C [42]. Further work by Asokan et al. on FeCrAl alloys at 600 °C suggests that Si promotes the Al activity in the alloy substrate, thereby greatly increasing the Al content of the primary protective oxide scale while reducing the Cr content, making it less susceptible to breakaway corrosion in presence of alkali and water vapor [74]. Therefore, the formation of the Al-rich protective oxide scale observed in the present studies could be attributed to two factors, namely the Si content in the alloy substrate and the exposure temperature (700 °C).

Despite the formation of a protective Al-rich oxide at 700 °C, it is evident that KOH(g) reacts with the alumina scale. In the presence of KOH, a 0.3 μm thick homogeneous layer consisting of K, O and Al was detected on top of the oxide scale (Fig. 12b). Formation of potassium aluminate such as $KAlO_2$ in association with alkali-induced corrosion on Al_2O_3 oxides has been discussed in previous studies [75,76]:

$$Al_2O_3(s) + 2KOH(g) \rightleftharpoons 2KAlO_2(s) + H_2O(g) \qquad \Delta G^0_{700^\circ C} = -237 kJ/mol \tag{R8}$$

Given the negative value of Gibbs free energy, it is argued that $KAlO_2$ is a possible candidate to be present on the oxide surface in the present envrionment. Nevertheless, Dahl et al. have suggested the formation of KAl_9O_{14} on top of an Al-rich oxide scale upon exposing a NiAl coating to humid air and KCl at 600 °C leaving the exact phase of the potassium aluminate found on the surface of EF101 uncertain [76]. Despite this uncertainty it is suggested that this corrosion product does not promote breakaway in the present environment, at least not after 168 h of exposure. Given the results presented in this paper, Kanthal® EF101 is considered a promising material for superheater application in the AR side of a CLC unit in respect of its corrosion-resistant properties.

6. Conclusions

This study offers insights into potential corrosion issues that may emerge on superheater tubes positioned in the AR side of a CLC unit that utilizes biomass as fuel. From a corrosion perspective, the week-long exposures at 700 °C reveal great potential in achieving high steam data and is in line with the state-of-the-art coal-fired boilers. Depending on the potential alkali load transferred from the FR to the AR, the possible selection of materials varies; in the absence of KOH(g), all investigated materials (stainless steels, Ni-base alloys and FeCrAl alloy) are suitable except for AISI 347H. In an environment with KOH(g) present, only the FeCrAl alloy Kanthal® EF101 obtained superior corrosion resistance, for up to 168 h.

The main findings of this work are highlighted below:

- AISI 347H underwent severe corrosion both in the presence and absence of KOH(g), characterized by the presence of thick internal oxidation zones and Fe-rich oxide scales. Furthermore, severe spallation was observed for this alloy upon cooling. These attributes combined make this material a poor choice for superheater material in the AR side of a CLC unit.
- In absence of KOH(g), local breakaway corrosion was observed on the austenitic stainless steels, Sanicro® 25 and AISI 310H argued to be related to Cr-evaporation. However, the corrosion rate was minor after 168 h of exposure and the oxide scales remained well-adherent to the alloy substrates. The Ni-base alloys Sanicro® 625 and Sanicro® 63x59 maintained a primary protective oxide scale after 168 h of exposure in absence of KOH(g).
- In the presence of KOH(g), a drastic increase of the corrosion rate of the chromia-forming alloys AISI 310H, Sanicro® 25, Sanicro® 625, and Sanicro® 63x59 was observed. This was attributed to the reaction of KOH(g) with the primary protective Cr-rich oxide scale, resulting in its rapid breakdown and the formation of K_2CrO_4 and a

less protective multilayered oxide scale. The corrosion attack was less severe for the Ni-based alloys compared to the stainless steels.

- A protective Al-rich oxide scale in the sub-micron range was formed on the FeCrAl alloy Kanthal® EF101 in both the clean and alkali slip scenario. It is argued that the oxide scale contains a low amount of Cr thereby preventing rapid breakdown of the primary protective oxide related to Cr-depletion via Cr-evaporation or formation of K_2CrO_4. Indication of potassium aluminate on top of the oxide scale was observed when exposed to KOH(g), with no signs of promoting breakaway corrosion.

CRediT authorship contribution statement

Hampus Lindmark: Writing – original draft, Methodology, Investigation, Data curation. **Robin Faust:** Writing – original draft, Investigation. **Tommy Sand:** Writing – review & editing. **Lars-Gunnar Johansson:** Writing – review & editing. **Pavleta Knutsson:** Writing – review & editing, Supervision, Funding acquisition, Conceptualization. **Jesper Liske:** Writing – review & editing, Supervision, Funding acquisition, Conceptualization.

Declaration of competing interest

The authors declare that they have no known competing financial interests or personal relationships that could have appeared to influence the work reported in this paper.

Data availability

Data will be made available on request.

Acknowledgement

This work was financed by the Swedish Energy Agency (projects P2020-004515 and P2018-90077) and The High Temperature Corrosion Center at Chalmers University of Technology.

This work was performed in part at the Chalmers Materials Analysis Laboratory, CMAL.

Appendix A. Supplementary material

Supplementary data to this article can be found online at https://doi.org/10.1016/j.fuel.2024.133178.

References

[1] Mbow H-OP, Reisinger A, Canadell J, O'Brien P. Special Report on climate change, desertification, land degradation, sustainable land management, food security, and greenhouse gas fluxes in terrestrial ecosystems (SR2). Ginevra, IPCC 2017;650.
[2] Shahbaz M, AlNouss A, Ghiat I, Mckay G, Mackey H, Elkhalifa S, et al. A comprehensive review of biomass based thermochemical conversion technologies integrated with CO2 capture and utilisation within BECCS networks. Resour Conserv Recycl 2021;173:105734.
[3] Masson-Delmotte V, Pörtner H-O, Skea J, Zhai P, Roberts D, Shukla PR, et al. Climate Change and Land: an IPCC special report on climate change, desertification, land degradation, sustainable land management, food security, and greenhouse gas fluxes in terrestrial ecosystems. 2019.
[4] Budinis S, Krevor S, Mac Dowell N, Brandon N, Hawkes A. An assessment of CCS costs, barriers and potential. Energ Strat Rev 2018;22:61–81.
[5] Brunetti A, Scura F, Barbieri G, Drioli E. Membrane technologies for CO2 separation. J Membr Sci 2010;359(1–2):115–25.
[6] Levihn F, Linde L, Gustafsson K, Dahlen E. Introducing BECCS through HPC to the research agenda: The case of combined heat and power in Stockholm. Energy Rep 2019;5:1381–9.
[7] Mikulčić H, Skov IR, Dominković DF, Alwi SRW, Manan ZA, Tan R, et al. Flexible Carbon Capture and Utilization technologies in future energy systems and the utilization pathways of captured CO2. Renew Sustain Energy Rev 2019;114:109338.
[8] Lyngfelt A. Chemical-looping combustion of solid fuels–status of development. Appl Energy 2014;113:1869–73.
[9] Rydén M, Lyngfelt A, Langørgen Ø, Larring Y, Brink A, Teir S, et al. Negative CO2 emissions with chemical-looping combustion of biomass–a Nordic energy research flagship project. Energy Procedia 2017;114:6074–82.
[10] Enestam S, Bankiewicz D, Tuiremo J, Mäkelä K, Hupa M. Are NaCl and KCl equally corrosive on superheater materials of steam boilers? Fuel 2013;104:294–306.
[11] Pettersson J, Folkeson N, Johansson L-G, Svensson J-E. The effects of KCl, K 2 SO 4 and K 2 CO 3 on the high temperature corrosion of a 304-type austenitic stainless steel. Oxid Met 2011;76(1):93–109.
[12] Ssenteza V, Eklund J, Hanif I, Liske J, Jonsson T. High temperature corrosion resistance of FeCr (Ni, Al) alloys as bulk/overlay weld coatings in the presence of KCl at 600° C. Corros Sci 2023;213:110896.
[13] Phother-Simon J, Jonsson T, Liske J. Continuous KCl addition in high temperature exposures of 304 L-A way to mimic a boiler environment. Corros Sci 2020;167:108511.
[14] Kinnunen H, Hedman M, Lindberg D, Enestam S, Yrjas P. Corrosion in recycled wood combustion—reasons, consequences, and solutions. Energy Fuel 2019;33(7):5859–66.
[15] Davidsson KO, Åmand L-E, Leckner B, Kovacevik B, Svane M, Hagström M, et al. Potassium, chlorine, and sulfur in ash, particles, deposits, and corrosion during wood combustion in a circulating fluidized-bed boiler. Energy Fuel 2007;21(1):71–81.
[16] Lehmusto J, Yrjas P, Skrifvars B-J, Hupa M. High temperature corrosion of superheater steels by KCl and K2CO3 under dry and wet conditions. Fuel Process Technol 2012;104:253–64.
[17] Okoro SC, Kiamehr S, Montgomery M, Frandsen FJ, Pantleon K. Effect of flue gas composition on deposit induced high temperature corrosion under laboratory conditions mimicking biomass firing. Part I: Exposures in oxidizing and chlorinating atmospheres. Mater Corros 2017;68(5):499–514.
[18] Okoro SC, Montgomery M, Frandsen FJ, Pantleon K. High temperature corrosion during biomass firing: improved understanding by depth resolved characterisation of corrosion products. Mater High Temp 2015;32(1–2):92–101.
[19] Sui J, Lehmusto J, Bergelin M, Hupa M. The Effects of KCl, NaCl and K 2 CO 3 on the high-temperature oxidation onset of sanicro 28 steel. Oxid Met 2016;85:565–98.
[20] Blomberg T, Tripathi T, Karppinen M. New chemical mechanism explaining the breakdown of protective oxides on high temperature steels in biomass combustion and gasification plants. RSC Adv 2019;9(18):10034–48.
[21] Demirbas A. Combustion of biomass. Energy Sources Part A 2007;29(6):549–61.
[22] Lyngfelt A, Pallares D, Linderholm C, Lind F, Thunman H, Leckner B. Achieving adequate circulation in chemical looping combustion— design proposal for a 200 mwth chemical looping combustion circulating fluidized bed boiler. Energy Fuel 2022;36(17):9588–615.
[23] Eriksson J-E, Zevenhoven M, Yrjas P, Brink A, Hupa L. Corrosion of heat transfer materials by potassium-contaminated ilmenite bed particles in chemical-looping combustion of biomass. Energies 2022;15(8):2740.
[24] Andersson V, Staničić I, Kong X, Leion H, Mattisson T, Pettersson JB. Alkali desorption from ilmenite oxygen carrier particles used in biomass combustion. Fuel 2024;359:130400.
[25] Gogolev I, Linderholm C, Gall D, Schmitz M, Mattisson T, Pettersson JB, et al. Chemical-looping combustion in a 100 kW unit using a mixture of synthetic and natural oxygen carriers–Operational results and fate of biomass fuel alkali. Int J Greenhouse Gas Control 2019;88:371–82.
[26] Gogolev I, Soleimanisalim AH, Mei D, Lyngfelt A. Effects of Temperature, Operation Mode, and Steam Concentration on Alkali Release in Chemical Looping Conversion of Biomass— Experimental Investigation in a 10 kWth Pilot. Energy Fuel 2022;36(17):9551–70.
[27] Gogolev I. Determining the Fate and Operational Implications of Alkalis in Chemical Looping Combustion of Biomass. Chalmers Tekniska Hogskola (Sweden) 2020.
[28] Kawahara Y. An overview on corrosion-resistant coating technologies in biomass/waste-to-energy plants in recent decades. Coatings 2016;6(3):34.
[29] Fantozzi D, Matikainen V, Uusitalo M, Koivuluoto H, Vuoristo P. Chlorine-induced high temperature corrosion of Inconel 625 sprayed coatings deposited with different thermal spray techniques. Surf Coat Technol 2017;318:233–43.
[30] Valiente Bermejo MA, Núñez AM, Norling R. Metal loss and corrosion attack of FeCrAl overlay welds on evaporator tube shields of a waste-fired power plant. Mater Corros 2024.
[31] Young DJ. High temperature oxidation and corrosion of metals. Elsevier; 2008.
[32] Zahs A, Spiegel M, Grabke HJ. Chloridation and oxidation of iron, chromium, nickel and their alloys in chloridizing and oxidizing atmospheres at 400–700 C. Corros Sci 2000;42(6):1093–122.
[33] Pettersson J, Svensson JE, Johansson LG. Alkali induced corrosion of 304-type austenitic stainless steel at 600 C; comparison between KCl, K2CO3 and K2SO4. *Materials science forum.* 595. Trans Tech Publ; 2008:367-75.
[34] Uusitalo M, Vuoristo P, Mäntylä T. High temperature corrosion of coatings and boiler steels below chlorine-containing salt deposits. Corros Sci 2004;46(6):1311–31.
[35] Persdotter A, Eklund J, Liske J, Jonsson T. Beyond breakaway corrosion–Influence of chromium, nickel and aluminum on corrosion of iron-based alloys at 600° C. Corros Sci 2020;177:108961.
[36] Phother-Simon J, Hanif I, Jonsson T, Liske J. High-Temperature Corrosion of P91/T91, 304l, Sanicro 28 and Inconel 625 Exposed at 600° C Under Continuous Kcl Deposition.
[37] Persdotter A, Eklund J, Liske J, Jonsson T. Beyond breakaway corrosion–Influence of chromium, nickel and aluminum on corrosion of iron-based alloys at 600 C. Corros Sci 2020;177:108961.

[38] Blomberg T. Correlation of the corrosion rates of steels in a straw fired boiler with the thermodynamically predicted trend of KOH (g) in the flue gases. Biomass Bioenergy 2012;39:489–93.
[39] Blomberg T. Which are the right test conditions for the simulation of high temperature alkali corrosion in biomass combustion? Mater Corros 2006;57(2):170–5.
[40] Blomberg T, Makkonen P, Hiltunen M. Role of alkali hydroxides in the fireside corrosion of heat transfer surfaces, a practical approach. *Materials Science Forum.* 461. Trans Tech Publ; 2004:883-90.
[41] Okoro SC, Montgomery M, Frandsen FJ, Pantleon K. Influence of preoxidation on high-temperature corrosion of a FeCrAl alloy under conditions relevant to biomass firing. Oxid Met 2018;89:99–122.
[42] Eklund J, Persdotter A, Ssenteza V, Jonsson T. The long-term corrosion behavior of FeCrAl (Si) alloys after breakaway oxidation at 600° C. Corros Sci 2023;217:111155.
[43] Nafari A, Nylund A. Field study on superheater tubes in the loop seal of a wood fired CFB plant. Mater Corros 2004;55(12):909–20.
[44] Eklund J, Paz MD, Jönsson B, Liske J, Svensson JE, Jonsson T. Field exposure of FeCrAl model alloys in a waste-fired boiler at 600° C: The influence of Cr and Si on the corrosion behaviour. Mater Corros 2019;70(8):1476–85.
[45] Lindmark H, Phother J, Olausson MDP, Nockert J, Lind F, Jonasson A, et al. A material degradation study of novel FeCrAl alloys, stainless steels and nickel base alloy in fluidized bed heat exchangers of a waste-fired CFB boiler. Fuel 2023;338:127299.
[46] Kofstad P. High temperature corrosion((Book)). London and New York, Elsevier Applied Science 1988;1988:568.
[47] Ssenteza V, Eklund J, Hanif I, Liske J, Jonsson T. High temperature corrosion resistance of FeCr (Ni, Al) alloys as bulk/overlay weld coatings in the presence of KCl at 600 C. Corros Sci 2023;213:110896.
[48] Nafari A, Nylund A. Erosion corrosion of steel tubes in the loop seal of a biofuel fired CFB plant. 2002.
[49] Eklund J, Jönsson B, Persdotter A, Liske J, Svensson J-E, Jonsson T. The influence of silicon on the corrosion properties of FeCrAl model alloys in oxidizing environments at 600 C. Corros Sci 2018;144:266–76.
[50] Nomoto H. Advanced ultra-supercritical pressure (A-USC) steam turbines and their combination with carbon capture and storage systems (CCS). Advances in Steam Turbines for Modern Power Plants. Elsevier 2017:501–19.
[51] Viswanathan R, Bakker W. Materials for ultrasupercritical coal power plants—Boiler materials: Part 1. J Mater Eng Perform 2001;10:81–95.
[52] Subcommittee A. Standard test methods for determining average grain size. ASTM international 1996.
[53] Halvarsson M, Tang JE, Asteman H, Svensson J-E, Johansson L-G. Microstructural investigation of the breakdown of the protective oxide scale on a 304 steel in the presence of oxygen and water vapour at 600 C. Corros Sci 2006;48(8):2014–35.
[54] Pint BA. Invited review paper in commemoration of over 50 years of oxidation of metals: addressing the role of water vapor on long-term stainless steel oxidation behavior. Oxid Met 2021;95(5):335–57.
[55] Asteman H, Segerdahl K, Svensson JE, Johansson LG. The influence of water vapor on the corrosion of chromia-forming steels. *Materials Science Forum.* 369. Trans Tech Publ; 2001:277-86.
[56] Asteman H, Svensson J-E, Johansson L-G, Norell M. Indication of chromium oxide hydroxide evaporation during oxidation of 304L at 873 K in the presence of 10% water vapor. Oxid Met 1999;52:95–111.
[57] Intiso L, Johansson L-G, Svensson J-E, Halvarsson M. Oxidation of Sanicro 25 (42Fe22Cr25NiWCuNbN) in O 2 and O 2+ H 2 O Environments at 600–750° C. Oxid Met 2015;83:367–91.
[58] Reddy MJ, Svensson J-E, Froitzheim J. Evaluating candidate materials for balance of plant components in SOFC: oxidation and Cr evaporation properties. Corros Sci 2021;190:109671.
[59] Asteman H, Svensson J-E, Norell M, Johansson L-G. Influence of water vapor and flow rate on the high-temperature oxidation of 304L; effect of chromium oxide hydroxide evaporation. Oxid Met 2000;54:11–26.
[60] Nicholls J, Evans H, Saunders S. Fracture and spallation of oxides. Mater High Temp 1997;14(1):5–13.
[61] Liu WN, Sun X, Stephens E, Khaleel M. Effect of substrate thickness on oxide scale spallation for solid oxide fuel cells. Corros Sci 2011;53(7):2406–12.
[62] Pettersson R, Enecker J, Liu L. Role of nickel in the oxidation of Fe–Cr–Ni alloys in air–water vapour atmospheres. Mater High Temp 2005;22(3–4):269–81.
[63] Pettersson R. Effects of composition on the corrosion of Fe–Ni–Cr alloys in chlorinating and sulfidising environments. Mater High Temp 2009;26(3):217–22.
[64] Götlind H, Liu F, Svensson J-E, Halvarsson M, Johansson L-G. The effect of water vapor on the initial stages of oxidation of the FeCrAl alloy Kanthal AF at 900 C. Oxid Met 2007;67:251–66.
[65] Sand T, Edgren A, Geers C, Asokan V, Eklund J, Helander T, et al. Exploring the effect of silicon on the high temperature corrosion of lean fecral alloys in humid air. Oxid Met 2021;95:221–38.
[66] Jonsson T, Froitzheim J, Pettersson J, Svensson J-E, Johansson L-G, Halvarsson M. The influence of KCl on the corrosion of an austenitic stainless steel (304L) in oxidizing humid conditions at 600 C: a microstructural study. Oxid Met 2009;72(3):213–39.
[67] Pettersson C, Pettersson J, Asteman H, Svensson J-E, Johansson L-G. KCl-induced high temperature corrosion of the austenitic Fe–Cr–Ni alloys 304L and Sanicro 28 at 600 C. Corros Sci 2006;48(6):1368–78.
[68] Jonsson T, Karlsson S, Hooshyar H, Sattari M, Liske J, Svensson J-E, et al. Oxidation after breakdown of the chromium-rich scale on stainless steels at high temperature: internal oxidation. Oxid Met 2016;85:509–36.
[69] Col A, Parry V, Pascal C. Oxidation of a Fe–18Cr–8Ni austenitic stainless steel at 850 C in O2: Microstructure evolution during breakaway oxidation. Corros Sci 2017;114:17–27.
[70] Ssenteza V, Eklund J, Bigdeli S, Jonsson T. Long-term corrosion behavior of FeCr (Al, Ni) alloys in O2+ H2O with KCl (s) at 600° C: Microstructural evolution after breakaway oxidation. Corros Sci 2024;226:111654.
[71] Izzuddin H, Hayashi S, Yoneda S, Kogin T, Ishikawa E, Noguchi M. Effect of Mo on corrosion behavior of Ni20Cr–xMo alloys in air with NaCl–KCl–CaCl2 vapor at 570° C. Mater Corros 2020;71(9):1488–99.
[72] Engkvist J, Canovic S, Liu F, Götlind H, Svensson J-E, Johansson L-G, et al. Oxidation of FeCrAl foils at 500–900 C in dry O2 and O2 with 40% H2O. Mater High Temp 2009;26(2):199–210.
[73] Josefsson H, Liu F, Svensson JE, Halvarsson M, Johansson LG. Oxidation of FeCrAl alloys at 500–900 C in dry O2. Mater Corros 2005;56(11):801–5.
[74] Asokan V, Eklund J, Bigdeli S, Jonsson T. The influence of Si on the primary protection of lean FeCrAl model alloys in O2 and O2+ H2O at 600 C—A microstructural investigation. Corros Sci 2021;179:109155.
[75] Wu D, Dahl K, Grumsen F, Christiansen T, Montgomery M, Hald J. Breakdown mechanism of γ-Al2O3 on Ni2Al3 coatings exposed in a biomass fired power plant. Corros Sci 2020;170:108583.
[76] Dahl KV, Slomian A, Lomholt TN, Kiamehr S, Grumsen FB, Montgomery M, et al. Characterization of pack cemented Ni2Al3 coating exposed to KCl (s) induced corrosion at 600° C. Mater High Temp 2018;35(1–3):267–74.